IEEE Access
Multidisciplinary | Rapid Review | Open Access Journal

Received April 9, 2019, accepted May 10, 2019, date of publication May 15, 2019, date of current version May 30, 2019.

Digital Object Identifier 10.1109/ACCESS.2019.2917070

Performance Evaluation of Multi-UAV System in Post-Disaster Application: Validated by HITL Simulator

MAHER ALJEHANI, (Student Member, IEEE), AND MASAHIRO INOUE, (Senior Member, IEEE)
Shibaura Institute of Technology, Saitama 337-8570, Japan

Corresponding author: Maher Aljehani (nb16507@shibaura-it.ac.jp)

This work was supported by the JSPS KAKENHI under Grant JP15k00929 and Grant JP19K0315.

ABSTRACT This paper proposes an evaluation of unmanned aerial vehicles (UAVs) performance in the mapping of disaster-struck areas. Sendai city in Japan, which was struck by the Tohoku earthquake/tsunami disaster in 2011, was mapped using multi-heterogeneous UAV. Normal mapping and searching missions are challenging as human resources are limited, and rescue teams are always needed to participate in disaster response mission. Mapping data and UAV performance evaluation will help rescuers to access and commence rescue operations in disaster-affected areas more effectively. Herein, flight plan designs are based on the information recorded after the disaster and on the mapping capabilities of the UAVs. The numerical and statistical results of the mapping missions were validated by executing the missions on real-time flight experiments in a simulator and analyzing the flight logs of the UAVs. After considering many factors and elements that affect the outcomes of the mapping mission, the authors provide a significant amount of useful data relevant to real UAV modules in the market. All flight plans were verified both manually and in a hardware-in-the-loop simulator developed by the authors. Most of the existing simulators support only a single UAV feature and have limited functionalities such as the ability to run different models on multiple UAVs. The simulator demonstrated the mapping and fine-tuned flight plans on an imported map of the disaster. As revealed in the experiments, the presented results and performance evaluations can effectively distribute different UAV models in post-disaster mapping missions.

INDEX TERMS Path planning evaluation, UAVs, mapping missions, disaster response, searching and rescue mission, flight plan design, hardware in the loop simulator.

I. INTRODUCTION

Unmanned aerial vehicles (UAVs) are a futuristic technology and a potential solution to many humanitarian problems. By virtue of their high-quality and low-cost sensors, UAVs have become a low-cost and accessible tool in academic and industrial research. Since their first deployment as air-force weapon systems in the early 1960s [1], UAVs have been continually developed for military operations. The technology was initially privatized by governments due to its expense and significant security threat. After 50 years of development, UAVs have entered the public domain, where they have been widely developed by universities, companies, and research centers. UAV deployment has now been extended to hobbies such as photography and racing, and to business applications such as agriculture, mapping, surveying, and delivery services. Furthermore, UAV can be merged with other technologies such as the internet of things (IoT), M2M communication systems, networking, functional control systems, system models, and satellite systems. Also, UAVs can contribute to mission-response assessment after a disaster. Specifically, impacted residential areas can be evaluated after a mapping mission. Damage evaluation relies on aerial and terrestrial images of the disaster-struck areas [2]. From these imagery data, an updated map (safe map) can be built and new rescue routes can be produced [3]. There are various UAV designs, each with a unique flight behavior [4]. Also, flight plan designs should consider UAV's mapping capabilities and area's features. This paper introduces system model and evaluations of flight performance of UAVs to map a disaster area in which based in two different types of UAVs on the market (i.e., fixed wing and multi-rotor designs) map the impacted areas in a disaster scenario in Japan [5]. The framework system model considers factors that influence the

The associate editor coordinating the review of this manuscript and approving it for publication was Zhen Li.

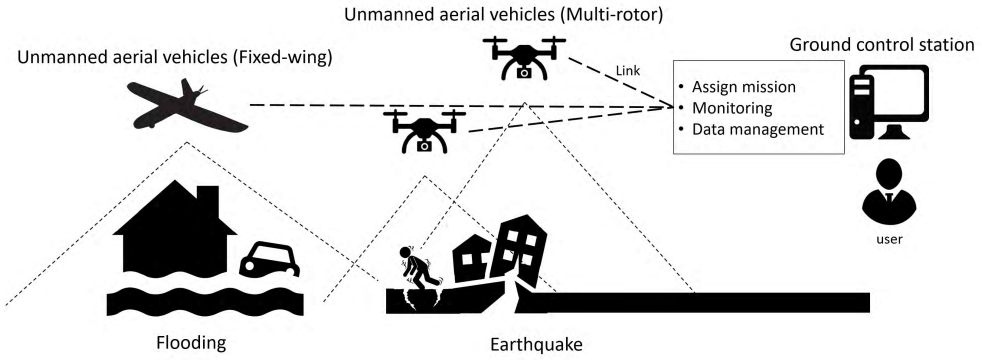

FIGURE 1. Scenario of a post-disaster mapping mission undertaken by fixed-winged and drone UAV models.

flight plan design. The experimental area had been stricken by the Tohoku earthquake and tsunami in 2011. Parts of the damaged areas are mapped by our system module, which was applied on our developed simulator. Figure 1 illustrates the surveying of the disaster area by the multi-UAV system.

The remainder of this paper is organized as follows, Section One continues below with an overview of related works and a formal problem statement. Section Two describes the system of the developed simulator, which is used in the results and experimental validation of the UAV system and Section Three presents the fine-tuning process UAV and camera specification. Section Four presents the experimental area and flight plan design. The experiments and their results are discussed in Section Five.

A. RELATED WORK

The deployment of multi-UAV systems in disaster response missions is a relatively innovative solution faced with many practical challenges, such as the effectiveness and stability of the operations during the mission, the network and communication system, the flight plan design, energy requirements, and mission management [6]. When integrating a multi-UAV system into a post-disaster application, the area of interest must be entirely covered. Coverage problems in static wireless sensor networks and the coverage enhancement of mobile nodes have been well researched in several studies [7]–[10]. Communication and networking (particularly the communication barriers) in UAV systems are discussed in depth in the next subsection. When planning the flight path of a UAV system with new modules, the designer must consider the high mobility and flight time while minding the limited battery life [11] The authors of [11] proposed two methods for tackling the dynamic coverage problem of multi-UAVs: dividing the area into subareas and planning the flight path of each UAV serving a designated sub-area in a two-dimensional scenario. Occlusion-awareness of a multi-UAV system has been addressed in [12]. However, the system in [12] covers a specific area and the waypoints are covered several times without considering the coverage quality. In another study, a flight plan for two-dimensional mapping was designed by a genetic algorithm [13]. This planning considers undiscovered obstacle environments and solves the optimization problem using stochastic methods. Energy consumption and the effectiveness of path planning have also been researched. The algorithm in [14], minimizes the energy consumption of UAVs deployed in missions. This algorithm considers the velocity and acceleration parameters of the mission and plans the path that best minimizes the energy consumption without affecting the missions' outcomes.

In autonomous missions, a UAV mainly uses its GPS and compasses to navigate the given waypoints. Real-time kinematic (RTK) GPS receivers can enhance the precision of GPS systems from meters (in conventional GPS) to centimeters. Other sensors that detect optical flow, ultrasonic, and distance (LIDARs) ensure a stable flight experience. In a related research project, Razi *et al.* [15] employed a UAV in a 3D photogrammetry technique that validates the methodology of monitoring an area. After mapping the land deformation and conducting a terrestrial survey, they reported more precise monitoring results by 3D photogrammetry than by Advanced Land Observation Satellite Phased Array L-band Synthetic Aperture Radar (ALSO PALSAR) [15]. Another study confirmed the excellent performance of UAVs in disaster recovery networks, regardless of whether the disaster is natural or man-made [16]. In that study, the multiple UAVs distributed in the disaster area acted as a relay between the surviving mobile-base stations. In [16] a stochastic geometric framework based on clustered deployment of drone small cells around the site of a destroyed base station is considered. The UAVs significantly enhanced the quality of information delivered to the ground users and the surviving base stations in post-disaster and other unforeseen events. UAVs are suitable not only for mapping and surveying missions, but also for tracking humans after a disaster [3], [17]. In [17], a group of UAVs semi-autonomously traced the paths of human refugees and generated escape routes based on their movements, while other groups of UAVs surveyed the area. Human planners then examined these routes along with aerial image data, and created a safe map. That safe map consists of new routes based on evaluation from aerial images. These images and highlighted routes can be uploaded to a social network service for easy access by endangered residents.

B. COMMUNICATION SYSTEM RELATED WORKS

Several investigations have focused on the communication systems of multi-UAV systems in post-disaster operations. Many considerations and scenarios must be addressed when developing communication systems. Fortunately, this problem has been well studied, and several frameworks, solutions, and system models have been proposed to overcome the communication delays in multi-UAV systems. The authors of [18] introduced a system model and flight mechanisms for wireless-enabled UAVs. They designed a communication system that collects information from the ground station under different considerations, such as power constraints and collision avoidance. Their iterative algorithm jointly optimizes the communication schedule, power allocation and flight plan designs to improve the performance between ground terminals. However, the UAVs altitude was fixed to the values that ensured collision avoidance of the UAVs. Delay between the ground control station (GCS) and online UAVs due to low bandwidth during the mission is another problem related to the communication system in various applications. The authors of [19] and [20] proposed an event-triggered heterogeneous nonlinear filter and a particle filter, respectively, for real-time dynamic estimation in wide-area measurement. With its nonlinear master-slave structure, the filter in [20] considers the communication and computation power generated from the node. This design delivers high accuracy while relieving the communication burden. Meanwhile, the event-triggered particle filter in [20] obtains the real-time state with suitable estimation accuracy, reduces the communication burden, and overcomes the limited transmission capability of UAVs in their network environment. Tuna *et al.* [21] proposed a UAV-aided emergency communication system and end-to-end communications in post-disaster scenarios. In experiments and simulations, the UAV-aided communication system proved its feasibility as a post-disaster emergency communications solution. UAVs can also be integrated with wireless sensor networks for natural disaster management. The main contributions of UAV, along with their unsolved challenges such as coverage, disconnectivity, security and privacy, and quality of service, are discussed in [22]. In a previous work, the authors combined three communications techniques into a hybrid communication system [17]. A default communication module (i.e., a cellular network) was configured with two communication modules (a wireless and a radio control module), which can be activated when the cellular network is unavailable. Additionally, if the communication has been intermittent throughout the mission, the system attempts to reconnect to the GCS via one of the communication methods. The communication system was manually selected by the user while considering the statuses of the available communication network(s). In such a case, the UAV executes the return to launch (RTL) point autonomously. The RTL can be configured in the flight controller used in the tested UAVs [23]. Similarly, the present paper considers the communication between UAVs and the GCS in the impacted area, and proposes a system model for UAV-based disaster missions.

C. POST-DISASTER SIMULATIONS

This subsection addresses the importance of simulations in disaster applications. A simulator helps to verify the system models in the post-disaster scenario. The authors of [24] deployed UAVs as a wireless sensor network in a post-disaster situation. Simulations are useful not only in communication scenarios but also for navigation and performance evaluations of disaster applications. For instance, the authors of [25] evaluated the efficiency and navigation performance of UAVs in a robotic simulator. By running artificial intelligence algorithms in the same simulator, they also established the UAV control settings that maximize the communication service coverage in a disaster scenario. Christy *et al.* [26] presented UAVs as a flying mobile-base tower station for device-to-device finding in a disaster area. In simulations, they verified that the flight plans were enhanced and that the coverage of the impacted area exceeded 80% with relatively low power consumption. As demonstrated in these examples, simulations are widely used in UAV-based post-disaster response, mapping, and communication. However, finding a suitable UAV (i.e., multi-UAV, customized camera, and UAV parameters) for a specific usage in disaster applications is a challenging task. Moreover, most of the existing simulators have limited functionalities for mapping-mission support. Therefore, their simulator was developed to verify the evaluation results of the UAV performance in the present study.

D. PROBLEM STATEMENT

Although many researches and studies have tested the practicality of deploying UAV systems in post-disaster response missions, flight planning considering capabilities of UAV's parameters needs further evaluation. Essential challenges of UAV's parameters need to discuss the efficiency of the flight performance and the number of UAV based on a scenario of disaster area. UAV's coverage capabilities must be analyzed statistically before implementation in the mission and the limit performance must be revealed to effectively map the area. Such system models and performance evaluations are missing and have not been systematically presented for heterogeneous UAV system. In an efficient flight plan, the UAVs should navigate only the critical areas, particularly in areas with a complex geometry accommodating various population distributions and natural areas. This study presents a system model and performance evaluations of two different types of UAVs on the market. An effective post-disaster flight plans have been implied considering communication range, GCS location, and disaster area data. Because preprocessing stages and simulators can help in verifying the system models, the authors evaluated the system model in a self-developed simulator operated in three–dimensional (3D) mode with different flight heights. Furthermore, numerical and statistical expressions were generated by implementing

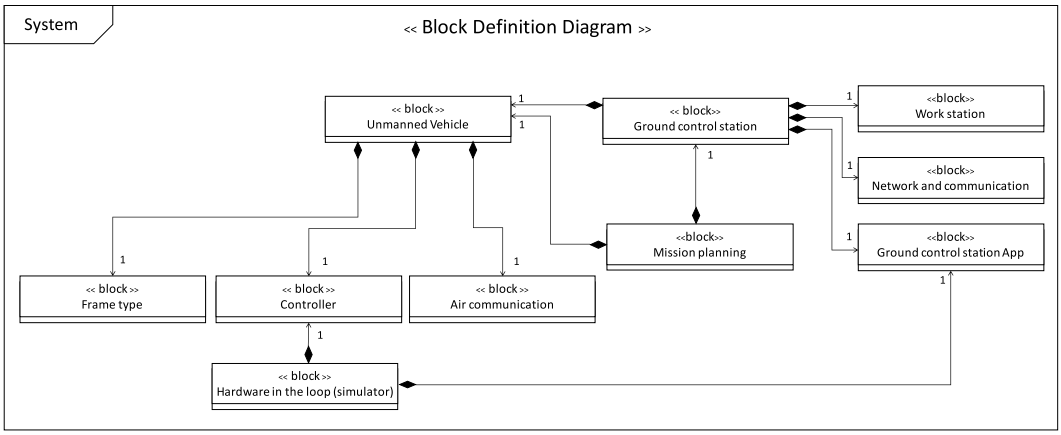

FIGURE 2. Block diagram showing the overall system-level design of the UAVs, HTL simulator and ground control station.

and fine-tuning the UAV parameters and selecting the camera specifications for mapping an area of interest. These parameters and specifications are based on real products on the market.

II. SYSTEM DESIGN

A. REQUIREMENTS

Before designing a system model, the system requirements must be determined in a preconditioning process [27]. This section outlines the system objectives from a development point of view, with reference to previous UAV implementations in disaster response planning. The purposes of the present study are listed below:

- Developing a cooperative multi-UAV system for post-disaster mapping missions.
- Selection different UAV models.
- Fine-tuning to minimize the flying time.
- Evaluating the UAV performance in the simulator.

B. HARDWARE IN THE LOOP SIMULATORS

Many hardware in the loop (HITL) simulators are available for testing UAV performances. However, most of these simulators do not provide multi-UAV options, and almost every simulator only tests the performance of a specific UAV model, which is impractical for evaluating different UAV models. To overcome this difficulty, the authors of [23] developed a HITL simulator based on a standard protocol (i.e., the MAVlink protocol). This simulator can simultaneously run two or more UAVs in one GCS workstation. Moreover, the default map can be updated by importing photographs, highlighted items, and map information into the simulator. The authors imported new map parameters from A geographic information system (GIS) like authors in their work [28], which provides frameworks of gathering and analyzing geography data. The simulator was developed in the C# programming language. Before demonstrating the multi-UAV system design in the HITL simulator, we must systematically define the UAV control and GCS. Figure 2 is a block definition diagram of the overall system design. The GCS application (GCSApp) transmits the commands and

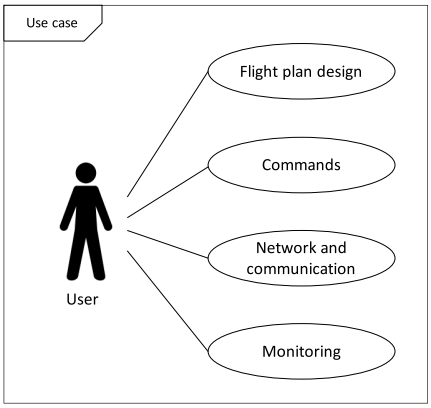

FIGURE 3. Schematic of a user and ground control station use case.

receives feedbacks from the UAVs and workstation (which can be a processing unit such as a computer or mobile device). The mission plan comprises flight strips, height, footprints, and the vehicle velocity. The controller on the UAV board is connected to multiple sensors inside the HITL simulator. The sensor data and disaster environment have been totally simulated in HITL, providing UAV feedback on a given map rather than sensor data in real flight. After designing the missions, the waypoints are uploaded and sent to the UAV controller through the network. The mission planning begins with the mission design and terminates after syncing the flight plans to the flight controller. The GCS stores the UAV flight data logs in the workstation and the flight controller storage. These data are sensor data provided by the HITL simulator (or by sensors in real flight experiments). The user (usually called the ground user) refers to the person or the pilot who controls the UAV, and designs the mission plans. The ground user has four main assignments: flight plan design, sending commands, managing the communications, and network and monitoring (see Figure 3).

C. GROUND CONTROL STATION

The main tasks of the GCS are controlling the UAVs and running the GCSApp to design the flight plans. The GCSApp

tool communicates with the UAV via a human–machine interface. Through the GCS unit, the ground user can control the UAVs, assign missions, and receive the telemetry data of the UAVs. The GCS unit performs multiple tasks as listed below:

- Managing the communications between the UAVs and GCSApp.
- Interfacing the control tools and sensors of the UAVs.
- Setting up the UAV parameters.
- Designing the UAV flight plan and manages missions.
- Sending commands and receiving information from a UAV.
- Monitoring the UAVs in real time.
- Analyzing and storing the videos and photographs which captured from the UAV.
- Processing the received data and analysis.
- Simulating the mission and presents its results before execution.
- Recording the flight logs of the mission and stores them in the workstation.

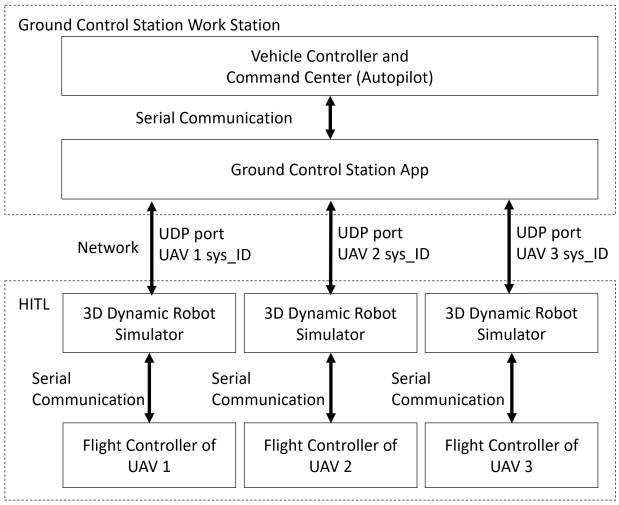

FIGURE 4. Developed HITL simulator for the multi-UAV system.

Figure 4 shows the HITL simulator developed by the authors. The UAVs are represented by 3D-dynamic robot simulators connected to one GCS. HITL simulator generates sensor data based on the UAV model parameters. To start the simulation, the HITL simulator must be simultaneously connected to the control unit and GCSApp. The three dynamic–robot simulators generate the sensor data in real time. Various algorithms, flight tests, and training of UAV systems can be implemented in the robot simulators in realistic scenarios. HITL simulators are connected to the GCSApp through serial ports. Although the HITL executes the mission on the controller unit, the feedbacks are simulated on the GCS or an external system with the same protocol as the flight controller. After executing the mission and receiving the simulated flight logs, the controller reports these data as telemetry data to the GCSApp, and displays the flight logs of the mission in real time

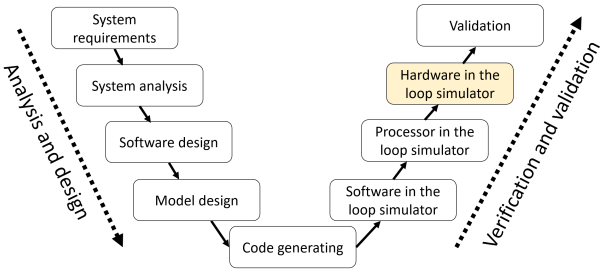

FIGURE 5. Model-Based Design (MBD).

As a system-level testing technique, the HITL simulator is applicable to realistic electronic components and embedded systems [29]. HITL simulation is one stage of model–based design; specifically, it validates the system requirements and tests the system design (see Figure 5). The HITL simulator runs commands into a gateway connected to the vehicle controller in real time, and displays the outputs. The technique can be used in systems of various complexity, from simple to very complicated. In the present study, the HITL simulator was developed for testing the multi-UAVs and flying designs. As HITL runs its commands on real hardware, it can evaluate a proposed system that cannot be tested easily, and verify the system outputs in realistic scenarios. When the vehicle flight controller connected to the GCSApp is provided with a vehicle simulator of the selected vehicle type, it is ready to receive commands from the GCSApp and execute commands. Thereafter, the HITL simulates the flight logs and sends its data to the controller. The simulator and GCSApp must be connected to the same network. The vehicle simulator provides the necessary feedbacks and displays them in the GCS interface. The more accurate the data from the simulator, the better are the validation results of the system.

In this study, all feedbacks were transmitted through User Datagram Protocol (UDP) protocols. The output data can also be configured to pass through the transmission control protocol [23]. The flight plan is transmitted to the vehicle controller through the network and GCS. The plan contains a series of waypoints and mission parameters such as velocity, altitude, acceleration and control mode. In all missions, the control mode was set to Autopilot. The UAV model must be known before sending the flight design to the vehicle controller. In this system, the GCS autonomously recognizes the UAV type at the instant of connecting the vehicle controller to the vehicle simulator. In real flight experiments, the GCS recognizes the UAV type from the vehicle controller, which has been configured to the UAV type before connection.

III. FLIGHT PLAN DESIGN

Fine-tuning in the flight design is the very important task before starting the mission. Generally, fine-tuning helps to complete the mission within the smallest time and require the fewest flight paths. On a polygon, fine-tune is characterized by two parameters, the number of turns w and the number of flight strips l. Figures 6 and 7 illustrate a non-fine-tuned and fine-tuned, respectively, on the same

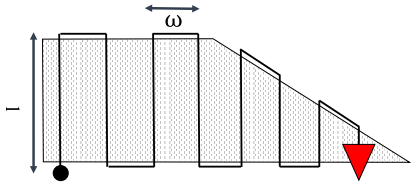

FIGURE 6. Example of polygon design without fine-tuning configuration over the disaster area (shaded polygon).

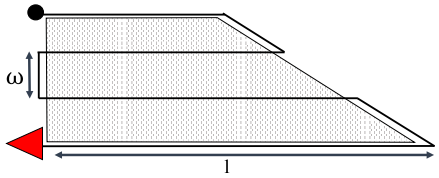

FIGURE 7. Example of fine-tuning the configuration over the disaster area (shaded polygon).

given polygon. When the mission takes many turns, the flight time is increased. For example, the suboptimal flight plan design in Figure 6 requires $w = 7$ turns and $l = 8$ strips.

In Figure 7 reduces these values to $w = 3$ and $l = 4$. Note that when the UAV flight strips are parallel to the longest line of the given rectangular polygon, the number of turns, and hence the number of flight strips, is reduced. When mapping a complex area, the polygon must sometimes be divided into multiple polygons and the flight must start from different points to minimize the w and l [30]. Before starting a flight plan design, the ground user requires the following specifications:

- The UAV models and their specifications (i.e., ground speed, maximum height, and flight behavior).
- The camera specifications (focal length, field of view (FOV), and ground sampling distance (GSD).
- The amount of overlap (end lap and side lap).
- Area size and status.

The data of aerial photogrammetry mappings are commonly collected from three FOVs: the true vertical FOV (from 0° up to ±3° from the nadir of the UAV), a lowly oblique FOV (*titled* photography; above ±3° but within ±30° of the nadir), and a highly oblique FOV (between ±35° and ±55° off-nadir). The present study adopts the vertical mapping orientation in all flight plan designs. When the UAV is dispatched to fly forward in the real experiments, a gimbal stabilizes to maintain a vertical camera view at all times.

A. PHOTOGRAMMETRIC OVERLAPS

Overlaps in the photogrammetric process are of two main types: end laps and side laps. The end lap represents the amount of data shared between images of photographic points along the flight strip, whereas the side lap describes the amount of data shared between images of adjacent flight strips. In typical cases, the end and side overlaps are 50–70% and 30–50%, respectively for fine-tuning [31]. Figure 8 demonstrates the end and side laps in the photogrammetric process of a rectangular polygon. In the experimental section

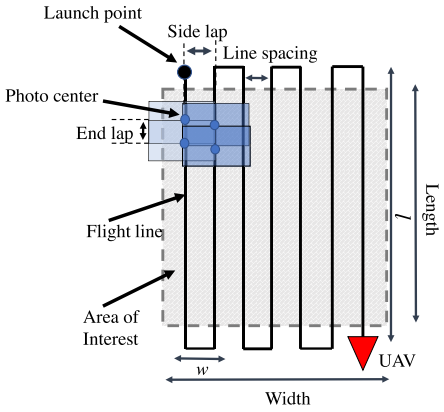

FIGURE 8. Overlaps in the mapping mission of a rectangular polygon using a vertical field of view.

TABLE 1. Camera specifications in the multi-rotor and fixed-wing frameworks.

Model	Multi-rotor	Fixed wing
Sensor type	CMOS	COMS
Focal length	8.8 mm	2.5 mm
Field of view (H) (h = 100 m)	600 m	1003.3 m
Field of view (V) (h = 100 m)	363.6 m	741.5m
Sensor size	13.2mm x 8mm	6.17mm x 4.56mm
Aspect ratios	4:3	4:3
Color filter type	RGB	RGB
Shutter type	Electronic / Mechanical	Electronic
Image resolution (Pixels)	5472 x 3078	4000 x 3000

of this study, the end and side laps are set to 70% and 50%, respectively.

B. GROUND SAMPLING DISTANCE

The flight plan design in the proposed framework considers the digital camera types. The camera model plays the main role in the flight plan design process, because the FOVs and GSD (which determines the resolution of the image) differ from one camera to another. A digital camera with a low FOV increases the w and time of the mission, whereas a camera with a high FOV decreases the w because the distance between lines is increased. A low GSD acquires high-quality images, but requires a heavy, expensive camera. Table 1 shows the camera specifications used in the two UAV models. The GSD is computed as follows:

$$GSD_h = \frac{h * \text{Sensor height}}{F_L * \text{Image height}} \quad (1)$$

$$GSD_w = \frac{h * \text{Sensor width}}{F_L * \text{Image width}} \quad (2)$$

where h is the UAV height and F_L represents the focal length (see Figure 9). In Table 1, the GSD of the digital camera was computed in both flight designs. For example, the GSD at $h = 400$ m is 11.81 cm/px for the multi-rotor camera and 24.72 cm/px for the fixed-wing camera. However, the fixed-wing camera offers a wider FOV than the multi-rotor camera, which reduces the number of flight strips in the mission. When computing the GSD, a designer must always consider

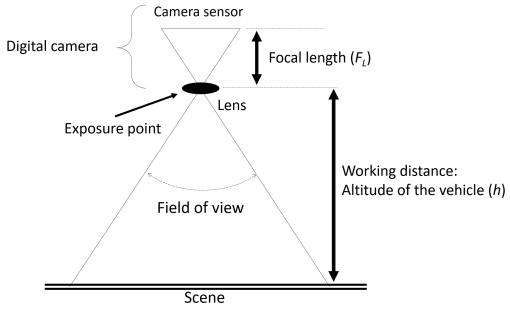

FIGURE 9. Focal length and flight height in the GSD computation.

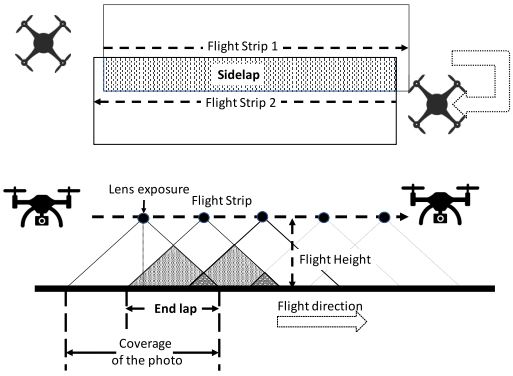

FIGURE 10. Operation of the multi-rotor framework in a mapping mission.

the worst-case scenario. For instance, if the GSD_h exceeds the GSD_w, the GSD_h should be considered in the flight plan design.

C. MULTI-ROTOR FRAMEWORK

The multi-rotor framework embraces several designs, for example, the quad-copter with four rotors, the hexa-copter with six motors, the octa-copter with eight motors, and the tri-copter with three motors and one servo. The quad, hexa, and octa multi-rotor can be configured in cross (x) or plus (+) forms. Among these designs, the quad-copter with the x configuration was simulated in the HITL. Unlike fixed-wing and helicopter model, multi-rotor are controlled by changing the motors' speeds to achieve 3D trajectory movements i.e., pitch, yaw, and roll [32]. When the multi-rotor copter reaches the end of a flight strip, it can yaw at an aggressive angle (see Figure 10). In contrast to its fixed-wing counterpart, the multi-rotor copter need not maintain its speed while executing roll, yaw or elevation maneuvers. The flexibility and maneuverability of multi-rotor frameworks are advantageous for mapping complex geometric areas.

D. FIXED-WING FRAMEWORK

Unlike the multi-rotor UAV, the fixed-wing vehicle can fly when air passes across its wings, creating an upward force on the wings that overcomes the downward pull of gravity. The three basic flying maneuvers, namely, roll, yaw, and pitch, are promoted by adjusting the wing angles [33]. However, the fixed-wing aircraft must maintain its speed while turning

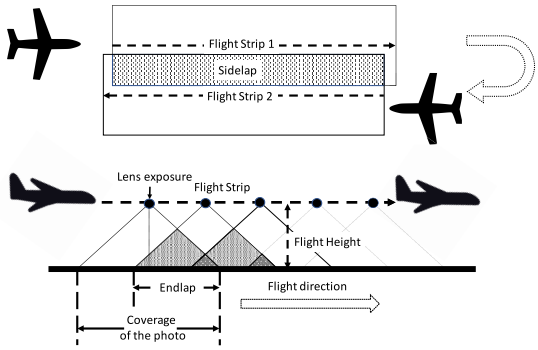

FIGURE 11. Operation of the fixed-wing framework in a mapping mission.

dynamically (see Figure 11). The advantages of the fixed wing over the multi-rotor framework are high velocity and rapid flight time. Therefore, fixed-wing aircraft are frequently deployed over wide areas.

E. SEQUENCE DIAGRAM OF THE MISSION DESIGN

Figure 12 shows the sequence diagram of the overall system, starting from the flight design and HITL execution, and concluding at the receipt and display of the flight logs of the mission. After establishing the connection between a UAV and GCSApp, Work_Station sends the command CMD_Plan_Design() to the ground user, granting permission to start designing the flight plan in GCSAp. GCSApp then confirms the requests via ACK_Plan_Design massages. The design process is begun in Plan_Design. During the flight plan design, GCSApp estimates the mission outcomes such as the flight time, visual trajectories, and footprints. The ground user uploads the completed flight plan design via the Upload_Flight_Design() command. GCSApp then processes the uploaded flight design and converts it into flight commands and a series of waypoints based on the protocol adopted by the UAV. In the next step, the flight design is synced with the UAV controller via the Sync_Flight_Design() message. In the present study, the UAVs adopt a serially communicated UDP protocol. All flight plan designs must begin with a Take Off command and end with a return to launch point (RTL). After the syncing process, the flight controller reforms the mission to suit the framework of the registered vehicle, and executes the mission commands in HITL. The mission is processed inside the HITL simulator, which produces telemetry data for the GCSApp. These data generate the flight logs of the vehicle's mission in real-time on a virtual map.

F. SYSTEM MODEL

This section discusses the problems of deploying UAVs in disaster applications. These problems are solved through system modeling of a multi-UAV system. Let u = UAV ($u > 1$ for a multi-UAV system) and g = GCS ($g = 1$ for a single GCS, or $g \geq 1$ for multiple GCSs). In this study, the application (post-disaster deployment) required a mobile GCS. The location of the GCS was denoted as

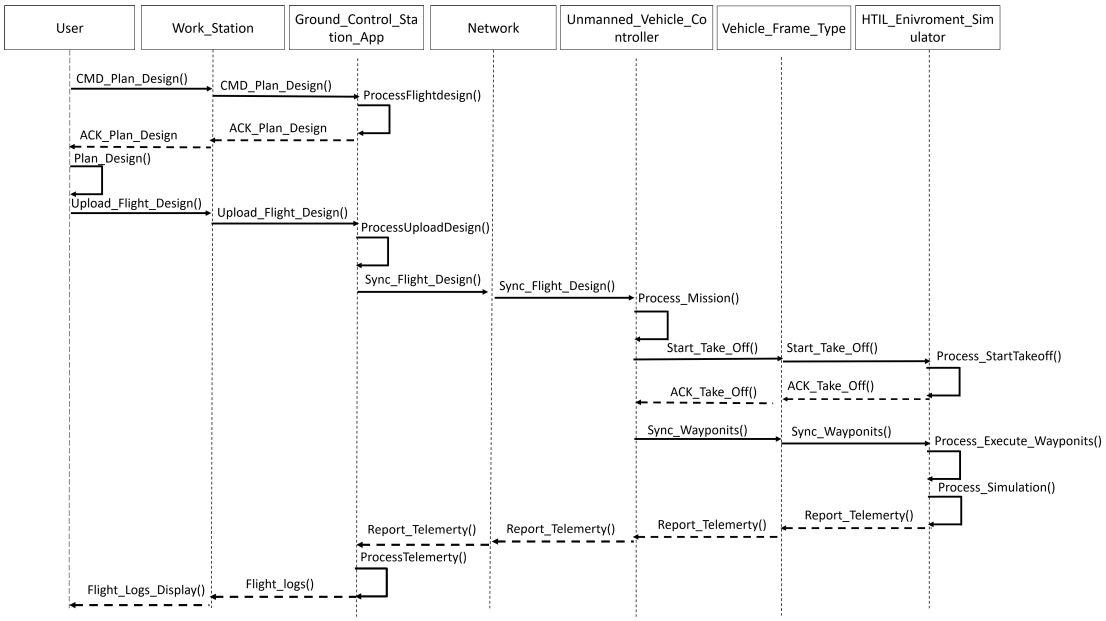

FIGURE 12. Sequence diagram of autonomous mission design and execution on the unmanned vehicles' flight controller and HITL simulator.

TABLE 2. Specifications of multi-rotor and fixed-wing vehicles.

Feature	Multi-rotor	Fixed-wing
Dimensions	289mm x 289mm x 196mm	1150mm x 580mm x 120mm
GPS	GPS+ rtk	GPS + rtk
Max flight time	28 minutes	45 minutes
Safe flight time	25:45 minutes	42:15 minutes
Velocity	22.3 m/s	25 m/s
weight+payload	1388g	900g

$\mathbf{w} = [x_g(t), y_g(t)]$ where is x_g and y_g are the GCS coordinates in the field at time instant t. Additionally, $0 \leq t \leq T_{(D)}$ where $T_{(D)}$ is the total period of the service. 3D modeling was applied to accommodate the varying flight height. In Cartesian coordinates, the 3D location of the UAV was expressed as ($m \in \mathrm{R}^3$) where is m represents the location of the UAV during the mission, given by

$$m = [x_u(t), y_u(t), h_u(t)], h_u(t) > 0, \tag{3}$$

where H_u is the altitude of the UAV, and x and z represent the UAV location from the FOV angle. The time t satisfies $0 \leq t \leq T_D$. T_D, where T_D is the overall mission time (including the takeoff time $T_{(TK)}$, the service (i.e., mapping) time $T_{(S)}$, and the time to back to the RTL point $T_{(RTL)}$. As the UAV will not take off unless the flight plan has been uploaded in the flight controller, the out-of-service time was ignored, and all missions were assumed to be completed successfully. The mission time was simply computed as follows:

$$T_{(D)} = T_{(TK)} + T_{(S)} + T_{(RTL)} \tag{4}$$

where T_D must be less than the maximum flight time (T_u) of the UAV (i.e., $T_D < T_{(u)\mathbf{MAX}}$). Herein, the maximum flight time of the UAVs is given in Table 2. The distance $d_{u,g}$ between a UAV and the GCS at time t t was calculated by Pythagoras' theorem in Cartesian coordinates:

$$d_{u,g}[t] = \sqrt{(x_u[t] - x_g[t])^2 + (y_u[t] - y_g[t])^2 + (h_u[t])^2} \tag{5}$$

The communication range of the GCS was denoted as β_g, with $\beta_g \leq \beta\mathrm{Max}$, and the area of interest was denoted by A. The GCS can locate outside the impacted area, but the communication must cover the area and collect the information from the UAVs during the mission. In particular, the GCS must locate within the UAV communication range. The GCS can communicate with the UAVs by several methods. The GCS–UAV communication is generally expressed as

$$\mathbf{w} \notin A \Rightarrow \beta_g \geq A \tag{6}$$

The distance between the UAV and GCS during the mission must not exceed the maximum range of the communication coverage at any instant. This constraint is given by

$$\forall d_{u,g}(t) \in \beta\mathbf{Max} \tag{7}$$

The UAV capabilities and flight times of the UAVs ($\mathbf{n}$) might be insufficient for mapping a large area. The number of UAVs that can be assigned to map A is calculated as follows:

$$\|\mathbf{n}\| = \left(\frac{A}{C_{(u)\mathbf{MAX}}}\right) + 1 \tag{8}$$

where $C_{(u)\mathbf{MAX}}$ represents the maximum coverage of the single UAV in mapping mission. It can be acquired from the flight logs results. Adding one more UAV is always appreciated in missions requiring fast completion. The times T_{TK}, T_S, and T_{RTL} differ among models with different UAV parameters and flight mechanisms, as explained in the flight design section. Therefore, further evaluation of the UAV performance is needed.

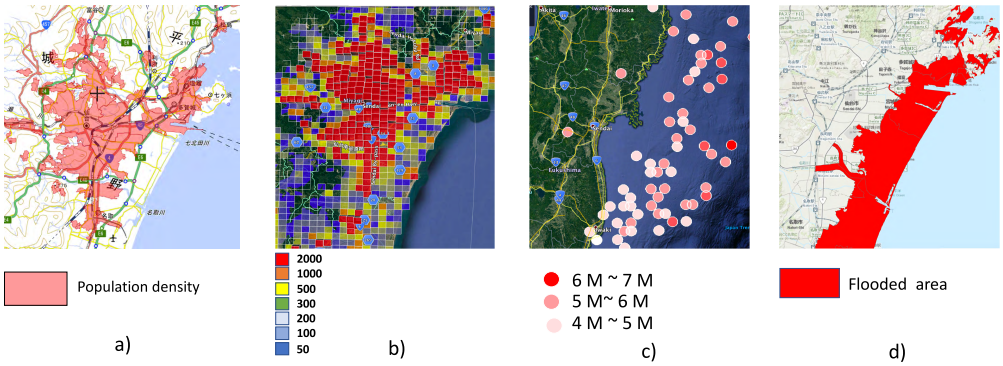

FIGURE 13. Area of Japan (Miyagi Prefecture) affected by the Tohoku earthquake and tsunami disaster of 2011: (a) Areal population density (2010), (b) Areal population distribution (2010), (c) Earthquake sites (2011), and (d) Areas flooded by the tsunami (2011).

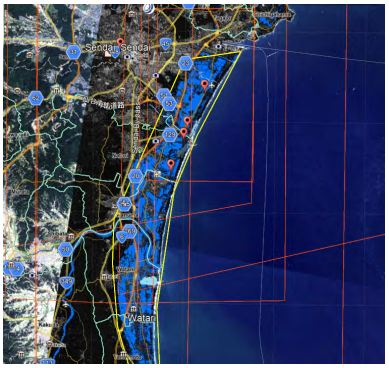

FIGURE 14. GSI monitors the land conditions imported into GCS map.

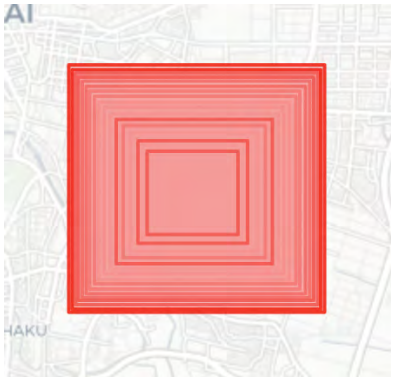

FIGURE 15. Area polygons designed inside the GCS map after importing GSI reports.

IV. IMPACTED AREA AND POLYGON DESIGNS

A. BACKGROUND OF THE EXPERIMENTAL AREA

A great earthquake struck the Pacific coast of Tohoku, Japan (38.1035° N, 142.861° E, M 9.0) at 14:46:18 JST. The earthquake was followed by a huge and devastating tsunami, causing 15,729 fatalities and 4,539 missing persons in the Hokkaido, Tohoku, and Kanto regions [5] (see Figures 13 and 14). Highways and railways were blocked and some were totally destroyed, preventing evacuees from leaving or reaching the nearest shelter. Nearly 5,200 spots were surveyed in the disaster area, providing one of the largest post-disaster datasets in surveying history [34]. The inundation height was surveyed by advanced instruments such as satellite systems, lasers, and GPSs. Based on the survey dataset, the maximum run-up height of the tsunami exceeded 10 m and was distributed along 500 km of coastline. The area affected by the 2011 event was the largest recorded in Tohoku's disaster history. Search and rescue teams, volunteers, and firefighters attempted to find survivors and access the impacted areas. However, as the routes were severely damaged and many areas were flooded, the disaster recovery required a prior mapping of the area and the identification of feasible entry routes. In such a scenario, a low-cost multi-UAV system contribution is invaluable for mapping and providing terrestrial and aerial images [35]. Therefore, the authors applied the proposed system model in the Tohoku disaster area and verified its performance in a simulator.

TABLE 3. Information of the affected area after the disaster.

Area Feature	Details
Assigned area name	Miyagi Prefecture, Sendai
Coordinates of the disaster Disaster type	38.1035° N, 142.861° E A strong earthquake of magnitude 9.0, causing a devastating 10–50 high m tsunami along 500 m of coastline
Time of the shock	14:46:18 JST
Damage distance	700 km
Aftershocks status	Additional 403 earthquakes, 32 with a magnitude greater than 6.0
Airport, railways and seaport status	Severely damaged

B. DESIGN POLYGONS

Table 2 lists the specifications of the UAVs deployed in this work, which are based on real commercial products. The UAV parameters were inserted in the HITL simulator. The pre-information and post-information data were then inserted into the map application of GCSApp. The tsunami, earthquake and population density data were imported from the Geospatial Information Authority of Japan (GSI) [36]. The GSI monitors the land conditions in Japan and provides the latest results of land surveys and disaster impacts. Figure 14 displays the post-disaster impact data imported into the map application. The polygon design is merely a rectangular design in GCS default map (See Figure 15).

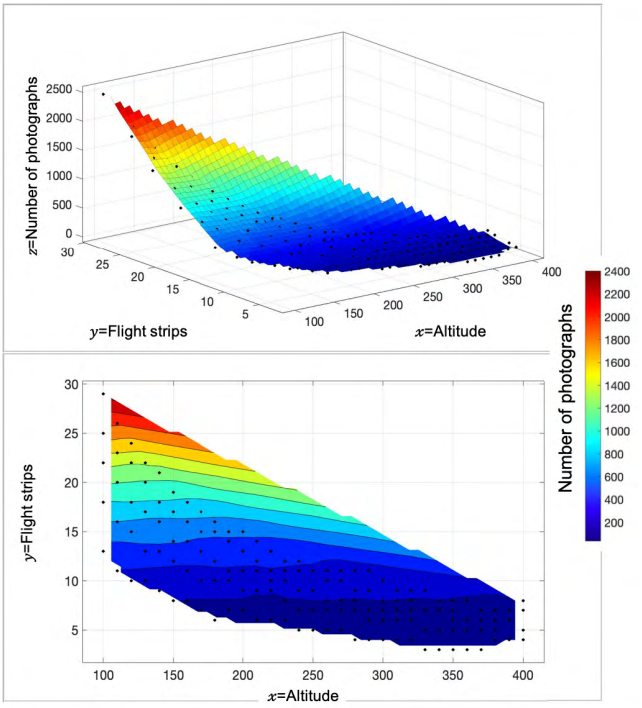

FIGURE 16. Relations among altitude, number of photographs and flight strips for the multi-rotor UAV in 3D view and down-view graphs.

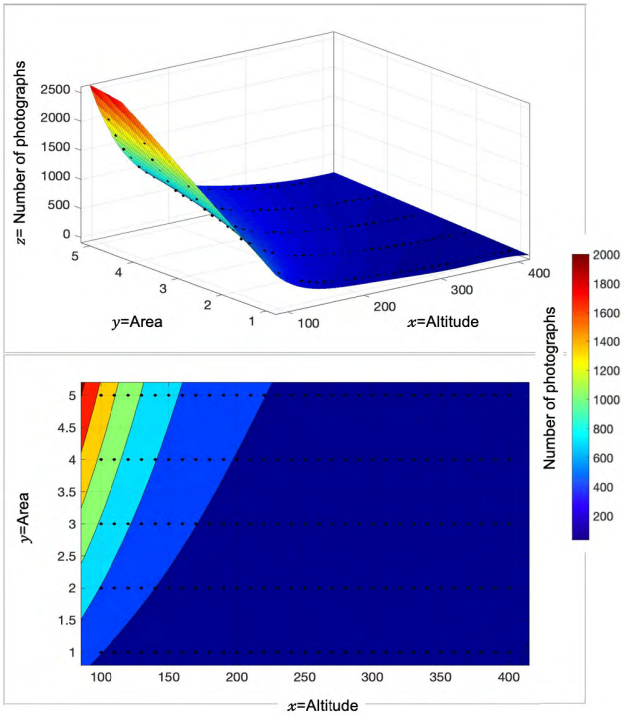

FIGURE 18. Relations among area, number of photographs and altitude for the multi-rotor UAV in 3D view and down-view graphs.

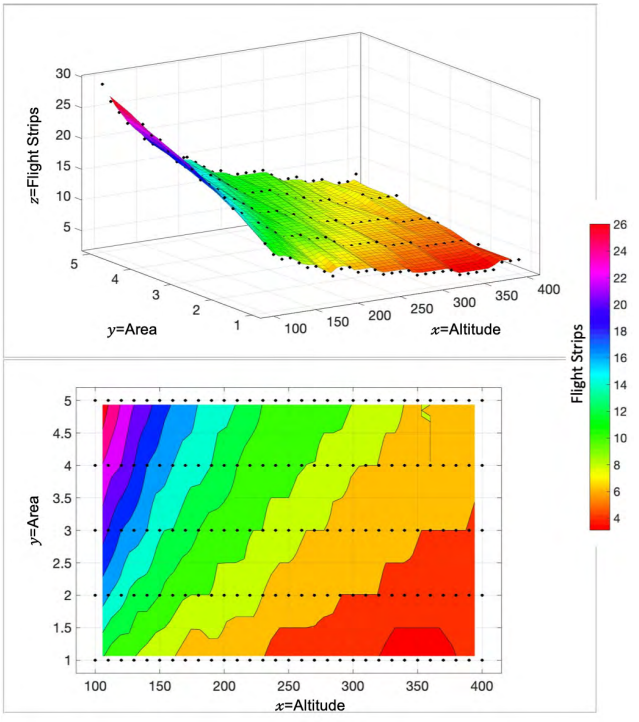

FIGURE 17. Relations among altitude, area and flight strips for the multi-rotor UAV in 3D view and down-view graphs.

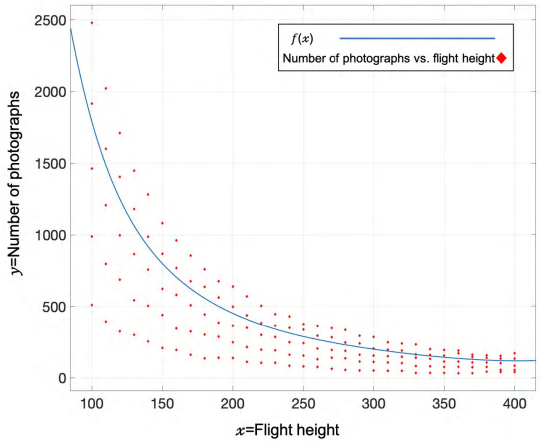

FIGURE 19. Relations among altitude and number of photographs for the multi-rotor UAV model. Where f(x) represents the non-robust residuals function and weighted by the area as shown in Table 4.

C. MISSION DESIGN AND EXECUTION

Polygons can be mapped by exact or approximate methods. It has been well researched in many studies [37]–[39], and [40]. The approximate method covers the region with a convex grid composed of a number of cells. The cell size depends on the coverage capabilities of the UAVs and the area of interest. The exact method decomposes the region into a set of polygonal subareas that exactly covers the original area. This study applies the approximate method because the area of interest has a very complex infrastructure. As the assigned area cannot be mapped by a single UAV with the specifications shown in Table 2, it was divided into sub-polygons that fit the UAVs capabilities. The polygons were designed manually and decomposed into a set of square designs to show the UAV performance in various

TABLE 4. Statistical evaluation of multi-rotor UAV performance based on 200 missions under different considerations of relations.

Simulation and relation	Type of data fitting	Sum squared error	R-Square	Adj R-sq	RMSE	Coefficients, functional expressions, and standard deviations of the analyzed flight results
Number of photographs, number of flight strips and altitude	Linear interpolation	2.2725e+03	0.9999	-	-	p = coefficient structure = 155, where is $f(x, y)$ = piece-wise linear surface computed from p coefficient where x is normalized by mean 250 and standard deviation 89.73 and where y is normalized by mean 10 and standard deviation 5.245
Number of flight strips, area and altitude	Linear interpolation	5.4431e–29	1	-	-	p = coefficient structure= 155 $f(x, y)$ = piece-wise linear surface computed from p = coefficient where x is normalized by mean 250 and standard deviation 89.73 and where y is normalized by mean 3 and standard deviation 1.419
Number of photographs, area and altitude	Polynomial with robust least absolute residuals (LAR) where $x = 5$ and $y = 1$ of $f(x, y)$	1.3618e+04	0.9995	0.9995	9.7247	p = coefficient structure = 11, Linear model Poly51: $f(x, y) = p00 + p10 * x + p01 * y + p20 * x^2 + p11 * x * y + p30 * x^3 + p21 * x^2 * y + p40 * x^4 + p31 * x^3 * y + p50 * x^5 + p41 * x^4 * y$ where x is normalized by mean 250 and standard deviation 89.73 and y is normalized by mean 3 and standard deviation 1.419. Coefficients (95% confidence bounds): p00 = 240.4 (237.5, 243.3) p10 = –173.8 (–180.7, –167) p01 = 112.8 (109.9, 115.7) p20 = 60.1 (53.97, 66.24) p11 = –64.91 (–68.81, –61.01) p30 = –32.82 (–41.92, –23.72) p21 = 36.35 (30.19, 42.51) p40 = 46.2 (43.89, 48.51) p31 = –42.06 (–44.06, –40.06) p50 = –17.59 (–20.29, –14.89) p41 = 18.12 (15.8, 20.44)
Number of photographs, and altitude weighted by area	Nine-degree polynomial with non-robust residuals $f(x)$	2.017e+07	0.7915	0.7786	389.6673	p = coefficient structure = 10 Linear model Poly9: $f(x) = p1 * x^9 + p2 * x^8 + p3 * x^7 + p4 * x^6 + p5 * x^5 + p6 * x^4 + p7 * x^3 + p8 * x^2 + p9 * x + p10$ where x is normalized by mean 250 and standard deviation 89.73. Coefficients (95% confidence bounds): p1 = 1.413 (–124.4, 127.2) p2 = 1.457 (–102.7, 105.6) p3 = –14.52 (–794.1, 765) p4 = 5.179 (–568, 578.3) p5 = 19.37 (–1610, 1648) p6 = 19.31 (–984.4, 1023) p7 = –78.15 (–1389, 1232) p8 = 112.4 (–489.4, 714.3) p9 = –202.8 (–535.3, 129.8) p10 = 289 (200.4, 377.5)

polygon design and different flight heights (See Figure 15) as described in the following process:

- Decompose the area into polygons that fit the UAV capabilities.
- Ignore the polygons covering natural areas (rivers, forests, mountains), and areas with no population.
- Distribute the GCSs on the area, such that each GCS serves the maximum number of polygons and is located at the nearest start point of its mission.
- Assign multi-rotor vehicles in missions requiring high-resolution images (complex geometries such as urban areas, small countryside areas, and areas needing many maneuvers). These data are available in the pre-information and post-information tables. If the area coverage exceeds 5.1 km^2 (the capability limit of mapping by multi-rotor vehicles), divide the polygon into multiple polygons.
- Assign fixed-wing UAVs in missions requiring a fast response over a wide area ($\geq$17 km^2). Fixed-wing UAV deployment is suitable for midtown areas, areas near the sea, flooded areas, and remote areas far from the GCS.

V. EXPERIMENTS

This section evaluates the performances of the UAVs in the simulator. The experimental results will help rescue teams and pilots to integrate the UAV(s) fulfilling the mapping mission requirements. For this purpose, the evaluation investigates many relations between the UAV parameters, and considers many factors: flight time, velocity, flight behavior (which influences the numbers of photographs and flight strips), camera specifications, fine-tuning, flight height, and area coverage. The values of these factors are based on those of marketed products. As the technical evaluations of marketed products are either missing or determined from few data, the performances of commercial UAVs are unclear. Herein, the relations between these factors were demonstrated statistically on graphs and based on multiple missions

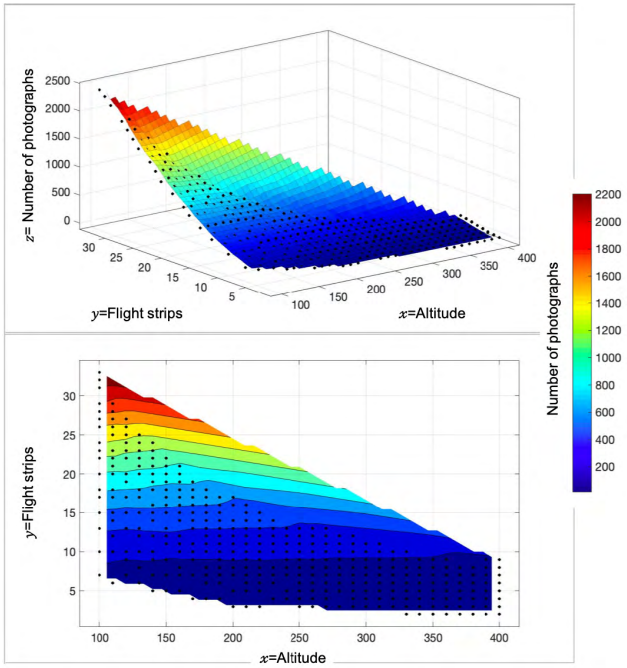

FIGURE 20. Relations among altitude, number of photographs and flight strips for the fixed-wing UAV in 3D view and down-view graphs.

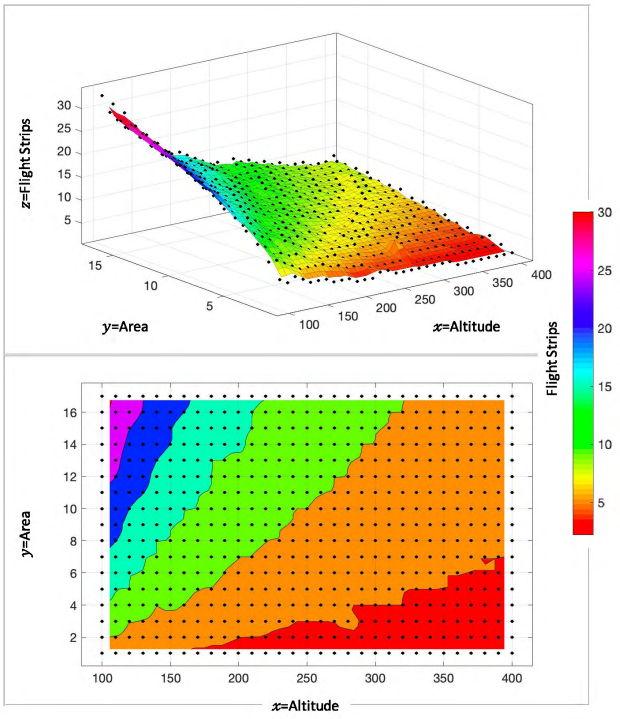

FIGURE 21. Relations among altitude, flight strips and area for the fixed-wing UAV in 3D view and down-view graphs.

in the simulator. The investigated factor relations are listed below:

- Number of flight strips, area, and flight height, investigated by linear interpolation.
- Number of photographs, number of flight strips, and area, investigated by linear interpolation.

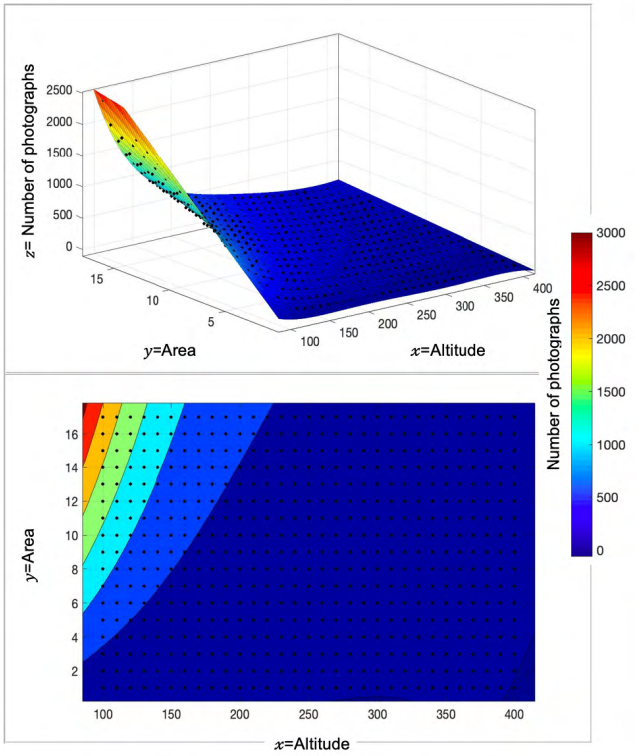

FIGURE 22. Relations among area, number of photographs and altitude for the fixed-wing UAV in 3D view and down-view graphs.

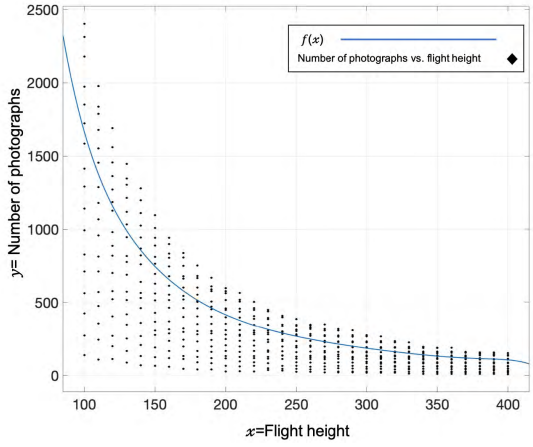

FIGURE 23. Relations among altitude and number of photographs for the fixed-wing UAV model. Where f(x) represents the non-robust residuals function and weighted by the area as shown in Table 5.

- Number of photographs, area, and flight height investigated by polynomial fitting with robust least absolute residuals (LAR).
- Number of photographs and flight height with area-weighted, investigated by non-robust polynomial fitting.

Functional expressions were generated for each relation. The authors executed 880 missions on the simulators (200 multi-rotor and 680 fixed-wing UAVs) with real flight times. The mission numbers were based on the UAVs' maximum mapping abilities over the given area (5 km and 17 km for the multi-rotor and fixed-wing UAVs, respectively).

TABLE 5. Statistical evaluation of the fixed-wing UAV performance based on 680 missions under different considerations of relations.

Simulation and relation	Type of data fitting	Sum squared error	R-Square	Adj R-sq	RMSE	Coefficients, functional expressions, and standard deviations of the analyzed flight results
Number of photographs, number of flight strips, and altitude	Linear interpolation	5.0985e+04	0.9994	-	-	p = coefficient structure = 523, $f(x, y)$ = piecewise linear surface computed from p coefficient where x is normalized by mean 250 and standard deviation 89.53 and where y is normalized by mean 10.37 and standard deviation 5.888
Number of flight strips, area and altitude	Linear interpolation	3.2974e–28	1	-	-	p = coefficient structure = 527, $f(x, y)$ = piecewise linear surface computed from p where x is normalized by mean 250 and standard deviation 89.53 and where y is normalized by mean 9 and standard deviation 4.904
Number of photographs, area and altitude	Polynomial with robust least absolute residuals (LARs), where $x = 5$ and $y = 1$ of $f(x, y)$	1.8719e+04	0.9998	0.9998	6.0231	p = coefficient structure = 11, Linear model Poly51: $f(x,y) = p00 + p10 * x + p01 * y + p20 * x^2 + p11 * x * y + p30 * x^3 + p21 * x^2 * y + p40 * x^4 + p31 * x^3 * y + p50 * x^5 + p41 * x^4 * y$ where x is normalized by mean 250 and standard deviation 89.73 and where y is normalized by mean 3 and standard deviation 1.419. Coefficients (with 95% confidence bounds): p00 = 1442 (1325, 1558) p10 = –35.2 (–37.84, –32.55) p01 = 564.3 (557.3, 571.2) p20 = 0.3234 (0.3005, 0.3463) p11 = –7.038 (–7.169, –6.907) p30 = –0.001407 (–0.001503, –0.001311) p21 = 0.03508 (0.03421, 0.03596) p40 = 2.918e–06 (2.723e–06, 3.114e–06) p31 = –7.898e–05 (–8.142e–05, –7.654e–05) p50 = –2.322e–09 (–2.476e–09, –2.167e–09) p41 = 6.653e–08 (6.41e–08, 6.896e–08)
Number of photographs, and altitude weighted by area	Nine-degree polynomial with non-robust residuals $f(x)$	2.0249e+08	0.7844	0.7806	625.8374	p = coefficient structure = 10 Linear model Poly9: $f(x) = p1 * x^9 + p2 * x^8 + p3 * x^7 + p4 * x^6 + p5 * x^5 + p6 * x^4 + p7 * x^3 + p8 * x^2 + p9 * x + p10$ where x is normalized by mean 250 and standard deviation 89.73 coefficients (with 95% confidence bounds): p1 = –2.254 (–63.85, 59.34) p2 = 3.193 (–47.91, 54.29) p3 = 5.729 (–377.7, 389.2) p4 = –5.947 (–288.5, 276.7) p5 = –11.94 (–816.9, 793) p6 = 35.76 (–461.4, 532.9) p7 = –61.48 (–712.1, 589.2) p8 = 96.04 (–203.4, 395.5) p9 = –185.6 (–351.4, –19.73) p10 = 267.8 (223.5, 312.1)

Therefore, in the polygon representation, the impacted area was expressed as $A = \{1, 2, \ldots 5\}$ for the multi-rotor UAVs and $A = \{1, 2, \ldots 17\}$ for the fixed-wing UAVs. The height h was varied as $100, 110, \ldots 400$. The velocity was set to its maximum value (22 m/s and 25 m/s for the multi-rotor and fixed-wing UAVs, respectively). All missions in the simulators were assumed to be successfully completed (i.e., with successful takeoff, mapping and landing), and the communication problem was within the range of β**Max** in the system model, as described in the previous subsection.

A. MULTI-ROTOR PERFORMANCE

This section evaluates the flight performances of the multi-rotor UAV model for different polygon sizes and flight heights over the impacted area. The polygon design methods and the experimental area were introduced in Section Four. Figure 16 relates the number of flight strips, number of photographs and flight heights for the multi-rotor UAV. The results are displayed as linear interpolations and contour plots. The black dots are the data sequences obtained from the HITL. The simulated velocity (set to the maximum velocity of the multi-rotor UAV as mentioned above) decreased during each turn of the UAV. The UAV performance as a function of area size and flight height is presented in Figure 17. Again, these graphs present the linear interpolation results and contour plots. The colors delineate the number of flight strips. Figure 18 relates the number of photographs, area, and altitude. Herein, the color range graduates the number of photographs. The data were fitted by a polynomial with robust LARs. Finally, Figure 19 plots the number of photographs versus the flight altitude, weighted by area. These data were fitted to a 9-degree polynomial (blue solid curve in the figure). The functional expressions of the multi-rotor relations in Figures 16–19, and their statistics, are presented in Table 4. The error sum of squares in Table 4 quantifies the divergence between the individual observation and the group mean. The coefficient of determination root square (R-squared) defines the proportionate

deviation in the variable y explained by the independent variables x in the linear regression model. The R-squared value is a property of the fitted model, and can be either unadjusted or adjusted (if the adjustment statistically improves the model performance) for the number of predictors in the model. The root mean squared error (RMSE) quantifies the deviation of the estimated values from the flight results. The last column in Table 4 presents the standard deviations, and the coefficients of the relations.

B. FIXED-WING PERFORMANCE

The flight times, flight behaviors (i.e., velocity, flight time, and turn angles), and camera specifications all differ among fixed-wing and multi-rotor UAV models. These differences are mainly responsible for the disparate results of fixed-wing and multi-rotor UAVs in autonomous mapping missions [4]. The specifications of both types were introduced and discussed in previous sections of this paper. Herein, the fixed-wing model has a maximum flight time of 45 min, a maximum velocity of 25 m/s, and an overall coverage ability of 17 km. All these factors were inserted manually to the simulator in each mission. Similar to the multi-rotor performance evaluations, the mapping results were displayed as contour plots, and the fixed-wing performances in the mapping missions were statistically expressed by linear interpolation or polynomial fitting. The number of flight strips, number of photographs and flight height are related in Figure 20. The black dots represent the data from the HITL simulator. Figure 21 coverage ability of 17 km. All these factors were inserted manually to the simulator in each mission. Similar to the multi-rotor performance evaluations, the mapping results were displayed as contour plots, and the fixed-wing performances in the mapping missions were statistically expressed by linear interpolation or polynomial fitting. The number of flight strips, number of photographs and flight height are related in Figure 20. The black dots represent the data from the HITL simulator. Figure 21 shows the fixed-wing performances over differently sized areas at different flight heights. Both figures display the linear interpolation results and contour plots. The number of photographs, coverage area, and altitude are related in Figure 22, where the colors delineate the number of photographs in the executed missions. The data were fitted to a polynomial with robust LARs. Figure 23 plots the number of photographs versus the flight altitude, weighted by area. These data were fitted to a 9-degree polynomial. The functional expressions of the fixed-wing UAV performances in Figures 20–23, and their statistics, are presented in Table 5.

VI. CONCLUSION

This study demonstrated the mapping performance of a multi-UAV system in a disaster-struck area of Japan. Experiments were conducted on a self-designed HITL simulator, a very realistic testing simulator that estimated the outcomes of the mapping missions. 880 missions have been executed in the simulator with real flight time consuming. The HITL simulator was constructed from 3D dynamic robot simulators, which replace real flight experiments. The GCSApp was connected to all UAVs at different ports. The simulator was run on two common UAVs with different camera specifications. Both UAV types (multi-rotor and fixed-wing) are based on currently commercial products. Based on the camera specifications, the ground surface distance was also determined for each type. This study confirmed the importance of UAV performance data to design flight plans. After defining the system objectives, the ground user can design polygons that meet the mapping capabilities of the UAVs considering communication and flight behaviors of each model. Multi-rotor UAVs are suitable for monitoring small urban areas, as their complexity and maneuverability enable obstacle avoidance in these areas. In flooded areas, areas far from the GCS, and remote areas, high maneuvers for avoiding obstacles are unnecessary. Such areas should be monitored by fixed-wing UAVs, which have longer flight times than multi-rotor UAVs. In this work, the flight plan design was based on UAV capabilities and area features. After executing the mapping mission in the HITL simulator, the performances of the UAVs were demonstrated in the flight logs generated during the mission. All mapping mission flight times included the takeoff, time of service and RTL time costs. The simulator can run multiple instances at the same time, enabling simultaneous mission executions, which is developed by the authors. The best-fit numerical expressions for both UAV types were derived by analyzing the flight logs of both UAV models while varying the number of photographs, number of flight strips, areal size, and altitude within the UAV and camera specifications. The 880 experimental mapping missions revealed the real performance of the UAVs. The empirical equations and statistical evaluations of the UAV performances were obtained in a HITL simulator. The obtained graphs and statistical results will help rescue teams and pilots to effectively deploy UAVs in disaster applications. The numerical and statistical performances of marketed UAVs are minimally provided or missing, impeding the effective application of UAVs in post-disaster mapping missions. Therefore, the marketed UAVs must be comprehensively evaluated in several time-consuming flight experiments. This study has highlighted the benefits of the simulator in performance evaluations of two different UAV models (based on their flight logs) under various considerations of mapping factors.

REFERENCES

[1] T. P. Ehrhard, "Air force UAV's: The secret history," Mitchell Inst. Airpower Studies, Arlington County, VA, USA, Tech. Rep., Jul. 2010.
[2] S. M. Adams and C. J. Friedland, "A survey of unmanned aerial vehicle (uav) usage for imagery collection in disaster research and management," in *Proc. 9th Int. Workshop Remote Sens. Disaster Response*, vol. 8, 2011, pp. 1–8.
[3] M. Aljehani and M. Inoue, "Multi-UAV tracking and scanning systems in M2M communication for disaster response," in *Proc. IEEE 5th Global Conf. Consum. Electron.*, Oct. 2016, pp. 1–2.
[4] M. Aljehani and M. Inoue, "Comparison of UAV flight behaviors after autonomous mapping of an urban area," in *Proc. IEEE 7th Global Conf. Consum. Electron. (GCCE)*, Oct. 2018, pp. 1–2.

[5] Y. Fujii, K. Satake, S. Sakai, M. Shinohara, and T. Kanazawa, "Tsunami source of the 2011 off the Pacific coast of Tohoku Earthquake," *Earth, Planets Space*, vol. 63, no. 7, p. 55, 2011.
[6] L. Gupta, R. Jain, and G. Vaszkun, "Survey of important issues in UAV communication networks," *IEEE Commun. Surveys Tuts.*, vol. 18, no. 2, pp. 1123–1152, 2nd Quart., 2016.
[7] G. Fan and S. Jin, "Coverage problem in wireless sensor network: A survey," *J. Netw.*, vol. 5, no. 9, pp. 1033–1040, 2010.
[8] R. Mulligan and H. M. Ammari, "Coverage in wireless sensor networks: A survey," *Netw. Protocols Algorithms*, vol. 2, no. 2, pp. 27–53, 2010.
[9] M. Vecchio, R. López-Valcarce, "Improving area coverage of wireless sensor networks via controllable mobile nodes: A greedy approach," *J. Netw. Comput. Appl.*, vol. 48, pp. 1–13, Feb. 2015.
[10] B. Liu, P. Brass, O. Dousse, P. Nain, and D. Towsley, "Mobility improves coverage of sensor networks," in *Proc. 6th ACM Int. Symp. Mobile Ad Hoc Netw. Comput.*, 2005, pp. pp. 300–308.
[11] Y. Chen, H. Zhang, and M. Xu, "The coverage problem in UAV network: A survey," in *Proc. 5th Int. Conf. Comput., Commun. Netw. Technol. (ICCCNT)*, Jul. 2014, pp. 1–5.
[12] M. Jakob, E. Semsch, D. Pavlicek, and M. Pechoucek, "Occlusion-aware multi-uav surveillance of multiple urban areas," in *Proc. 6th Workshop Agents Traffic Transp. (ATT)*, 2010, pp. 59–66.
[13] S.-Y. Fu, L.-W. Han, Y. Tian, and G.-S. Yang, "Path planning for unmanned aerial vehicle based on genetic algorithm," in *Proc. IEEE 11th Int. Conf. Cogn. Inform. Cogn. Comput.*, Aug. 2012, pp. 140–144.
[14] C. Di Franco and G. Buttazzo, "Energy-aware coverage path planning of UAVs," in *Proc. IEEE Int. Conf. Auto. Robot Syst. Competitions*, Apr. 2015, pp. 111–117.
[15] P. Razi, J. T. S. Sumantyo, D. Perissin, H. Kuze, M. Y. Chua, and G. F. Panggabean, "3D land mapping and land deformation monitoring using persistent scatterer interferometry (PSI) ALOS PALSAR: Validated by geodetic GPS and UAV," *IEEE Access*, vol. 6, pp. 12395–12404, 2018.
[16] A. M. Hayajneh, S. A. R. Zaidi, D. C. McLernon, M. Di Renzo, and M. Ghogho, "Performance analysis of uav enabled disaster recovery networks: A stochastic geometric framework based on cluster processes," *IEEE Access*, vol. 6, pp. 26215–26230, 2018.
[17] M. Aljehani and M. Inoue, "Safe map generation after a disaster, assisted by an unmanned aerial vehicle tracking system," *IEEJ Trans. Electr. Electron. Eng.*, vol. 14, no. 2, pp. 271–282, 2019.
[18] Y. Xu, L. Xiao, D. Yang, Q. Wu, and L. Cuthbert, "Throughput maximization in multi-UAV enabled communication systems with difference consideration," *IEEE Access*, vol. 6, pp. 55291–55301, 2018.
[19] S. Li *et al.*, "Event-trigger heterogeneous nonlinear filter for wide-area measurement systems in power grid," *IEEE Trans. Smart Grid*, vol. 10, no. 3, pp. 2752–2764, May 2018.
[20] X. Liu *et al.*, "Event-trigger particle filter for smart grids with limited communication bandwidth infrastructure," *IEEE Trans. Smart Grid*, vol. 9, no. 6, pp. 6918–6928, Nov. 2018.
[21] G. Tuna, B. Nefzi, and G. Conte, "Unmanned aerial vehicle-aided communications system for disaster recovery," *J. Netw. Comput. Appl.*, vol. 41, pp. 27–36, May 2014.
[22] M. Erdelj, M. Król, and E. Natalizio, "Wireless sensor networks and multi-UAV systems for natural disaster management," *Comput. Netw.*, vol. 124, pp. 72–86, Sep. 2017.
[23] L. Meier *et al.* (2013). *MAVLink: Micro Air Vehicle Communication Protocol*. [Online]. Available: http://qgroundcontrol.org/mavlink/start.[Hämtad 2014-05-22]
[24] G. Tuna, T. V. Mumcu, K. Gulez, V. C. Gungor, and H. Erturk, "Unmanned aerial vehicle-aided wireless sensor network deployment system for post-disaster monitoring," in *Emerging Intelligent Computing Technology and Applications* (Communications in Computer and Information Science), vol. 304, D. S. Huang, P. Gupta, X. Zhang, and P. Premaratne, Eds. Berlin, Germany: Springer, 2012. [Online]. Available: https://link.springer.com/chapter/10.1007/978-3-642-31837-5_44
[25] J. Sánchez-García, J. M. García-Campos, S. Toral, D. Reina, and F. Barrero, "An intelligent strategy for tactical movements of UAVs in disaster scenarios," *Int. J. Distrib. Sensor Netw. Arch.*, vol. 2016. New York, NY, USA: Hindawi Publishing Corp., Mar. 2016, Art. no. 18.
[26] E. Christy, R. P. Astuti, B. Syihabuddin, B. Narottama, O. Rhesa, and F. Rachmawati, "Optimum UAV flying path for device-to-device communications in disaster area," in *Proc. Int. Conf. Signals Syst. (ICSigSys)*, May 2017, pp. 318–322.
[27] B. Nuseibeh and S. Easterbrook, "Requirements engineering: A roadmap," in *Proc. Conf. Future Softw. Eng.*, 2000, pp. 35–46.
[28] T. Nagata, Y. Kimura, and M. Ishii, "Use of a geographic information system (GIS) in the medical response to the Fukushima nuclear disaster in Japan," *Prehospital Disaster Med.*, vol. 27, no. 2, pp. 213–215, Apr. 2012.
[29] J. A. Ledin, "Hardware-in-the-loop simulation," *Embedded Syst. Program.*, vol. 12, pp. 42–62, Feb. 1999.
[30] Y. Li, H. Chen, M. J. Er, and X. Wang, "Coverage path planning for UAVs based on enhanced exact cellular decomposition method," *Mechatronics*, vol. 21, no. 5, pp. 876–885, Aug. 2011.
[31] P. R. Wolf and B. A. Dewitt, *Elements of Photogrammetry: With Applications in GIS*, vol. 3. New York, NY, USA: McGraw-Hill, 2000.
[32] Y.-J. Tsai, C.-S. Lee, C.-L. Lin, and C.-H. Huang, "Development of flight path planning for multirotor aerial vehicles," *Aerospace*, vol. 2, no. 2, pp. 171–188, 2015.
[33] M. Pepe, L. Fregonese, and M. Scaioni, "Planning airborne photogrammetry and remote-sensing missions with modern platforms and sensors," *Eur. J. Remote Sens.*, vol. 51, no. 1, pp. 412–436, 2018.
[34] N. Mori, T. Takahashi, and Tohoku Earthquake Tsunami Joint Survey Group, "Nationwide post event survey and analysis of the 2011 Tohoku earthquake tsunami," *Coastal Eng. J.*, vol. 54, no. 1, 2012, Art. no. 1250001.
[35] M. Aljehani and M. Inoue, "Communication and autonomous control of multi-UAV system in disaster response tasks," in *Proc. KES Int. Symp. Agent Multi-Agent Syst., Technol. Appl.* Springer, 2017, pp. 123–132.
[36] A. Zerger and D. I. Smith, "Impediments to using GIS for real-time disaster decision support," *Comput., Environ. Urban Syst.*, vol. 27, no. 2, pp. 123–141, Mar. 2003.
[37] B. J. Bulušek, "Coverage path planning in non-convex polygon areas for orthophotomap creation using UAVs," in *Proc. Conf. IEEE*, vol. 111, 2015, p. 117.
[38] E. Santamaria, F. Segor, I. Tchouchenkov, and R. Schönbein, "Rapid aerial mapping with multiple heterogeneous unmanned vehicles," in *Proc. ISCRAM*, 2013, pp. 1–10.
[39] L. H. Nam, L. Huang, X. Li, and J. F. Xu, "An approach for coverage path planning for UAVs," in *Proc. IEEE 14th Int. Workshop Adv. Motion Control (AMC)*, Apr. 2016, pp. 411–416.
[40] N. Dadkhah and B. Mettler, "Survey of motion planning literature in the presence of uncertainty: Considerations for UAV guidance," *J. Intell. Robot. Syst.*, vol. 65, no. 1, pp. 233–246, 2012.

MAHER ALJEHANI received the B.E. degree in telecommunication engineering from the Huazhong University of Science and Technology, the Associate degree in telecommunication from the Jeddah College of Telecom and Electronics, and the M.S. degree in systems engineering and science from the Shibaura Institute of Technology, in 2016, where he is currently pursuing the Ph.D. degree with the Department of Communication Function Control Engineering. He has been engaged in UAV Research Fields, since 2014 and a Research Visitor with Valley Campus Japan Inc. He is a Student Member of IEEE and a Young Professional Member.

MASAHIRO INOUE received the B.S. and M.S. degrees in pure and applied physics from Waseda University, and the Ph.D. degree in computer science from Shizuoka University. He was engaged in research and development with Mitsubishi Electric Corporation. Since 2005, he has been a Professor with the Department of Electronic Information Systems, College of Systems Engineering and Science, Shibaura Institute of Technology. Since 2017, he has been the Vice President of the Shibaura Institute of Technology. He is a Senior Member of IEEE.